Full Length Article

Corrosion resistance of tungsten carbide-rich coating layers produced by noble gas ion mixing

A.S. Racz, Z. Kerner, M. Menyhard [*]

Centre for Energy Research, Konkoly Thege M. út 29-33, H-1121 Budapest, Hungary

ABSTRACT

Tungsten carbide (WC) belongs to the class of protective coatings due to its good mechanical properties and corrosion resistance. Herein WC-rich coating layers have been produced by irradiating C/W multilayers with noble gases at room temperature. The in-depth concentration distributions after ion irradiation have been measured by Auger electron spectroscopy depth profiling. The corrosion resistance of the formed layers has been tested in 3.5 wt% NaCl solution. It has been shown that the growth of the WC-rich layer started at the interfaces and with increasing fluence the separately growing layers coalesced. With the coalescence of the layers the corrosion resistance of the system suddenly increased. To describe this phenomenon the term effective areal density has been introduced. If the effective areal densities of WC were lower and higher than 550 $(1/nm^2)$ and 1200 $(1/nm^2)$, the corrosion current densities were 0.5 and 0.08 $(\mu A/cm^2)$, resp. The in-depth distribution of the WC-rich layer and thus the corrosion resistance could be tailored by varying the projectiles, fluences, energies and initial layer structure. The maximum corrosion resistance found was better than that of stainless steel and WC cermet. The effective areal densities could be predicted by TRIDYN simulations allowing the design of corrosion resistive coatings.

1. Introduction

There is always a need for materials with exceptional mechanical durability and chemical resistance. Candidate materials with superior mechanical durability and chemical resistance among others are Ti and Si based nitrides (TiN and Si_3N_4), and various carbides (SiC, ZrC, and WC). Tungsten-carbide is widely used in numerous harsh applications, owing to its very high hardness and exceptional inertness to chemical attack. Specifically, WC is one of the most favorable choices for modern cemented coatings [1]. It has been widely used in numerous harsh applications as protective coatings due to their good mechanical properties: high hardness and good corrosion resistance and low wear properties, that are sustained up to 400 °C [2,3]. As a composite coating WC has been used to improve the tribological properties of diamond-like carbon and amorphous carbon coatings [1,4,5]. It can be applied both as individual or composite coating serving as a protective layer on stainless steel or aluminum alloys [1,6]. As a cermet its corrosion resistance is poor due the presence of the cobalt binder. Thus, Co was tried to be replaced by other binders like Ni or Cr; other solution like binderless carbides are still researched [7,8].

Different processes have been used for depositing WC coatings like plasma spraying, physical vapor deposition (PVD) and chemical vapor deposition (CVD). Typically, CVD processes are carried out at temperatures above 500 °C, which does not allow the coatings to be applied on hardened steels without significantly affecting the substrate's mechanical properties [2]. PVD processes offer low temperature deposition but it often leaves high compressive residual stress and stress gradient in the sample which can lead to the delamination of the coating [9,10]. Ion irradiation based methods are also available for producing coating layers. It has been shown that appropriate ion irradiation may increase the wear and corrosion resistance of the materials. For example it has been shown that tungsten implantation to steel increased the wear [11]. An interesting process has been published by Liu et al. [12]. To improve the adhesion of the a-C on steel the steel was irradiated by 20 keV, $5 \times 10^{17} W^+/cm^2$. The a-C was evaporated on the pre-implanted steel. At the interface WC + C layer formed and besides the improved adhesion the corrosion resistance was also improved [12].

It has been known for a long time that during ion bombardment ion beam mixing (IBM) happens [13]. During IBM compound formation may also occur; as it is a non-equilibrium process it also can be applied to

---

produce high heat of formation compounds at room temperature. Several authors have demonstrated IBM-induced compound formation in case of multilayer structures. Galindo et al. produced chromium-silicon mixed oxides by mixing of Cr/Si bilayer by oxygen atoms [14]. Gupta et al. synthetized PbTe nanocrystals using low energy ion beam mixing of a Te/Pb bilayer on a Si substrate [15]. Arranz et al. investigated the mixing of Ti and Si layers [16]. Harbsmeier et al. have shown that ion bombardment can induce solid state reaction in Si&C mixture [17]. Racz et al. showed that SiC nano-layer can be produced by IBM at room temperature [18,19].

Theoretically other carbides can also be produced at room temperature by IBM by irradiating metal/C layer structures. Herein it will be demonstrated that by applying IBM binderless WC coating layers can be produced. Noble gas (energy range 40–120 keV) ions induced ion beam mixing in C/W multilayer systems and subsequent compound formation happened as well. It will be shown that WC-rich layer of desired thickness and composition can be produced this way by changing the ion energy, fluence and initial layer thicknesses. The distribution of the elements and WC after irradiation is analyzed by Auger electron spectroscopy (AES) depth profiling. The chemical resistance of the irradiated sample is tested by potentiodynamic corrosion test which was better than commercially known materials e.g. stainless steel, WC cermet. It turned out that our previously introduced quantity the effective areal density [18,20] with slight modification could be also used here to characterize the chemical resistance of the samples. It had been shown that though the ion beam mixing of the Si/C and W/C systems are strongly different being ballistic and thermal spike, resp. doing some parametrization the TRIDYN simulation [21] is still able to estimate the in-depth distribution of elements after irradiation [22] and a simple model provides the amount of WC and the effective areal density can be calculated as well. These findings show the possibility of the design of the corrosion resistant coatings by the help of TRIDYN simulation.

2. Experimental section

2.1. Producing WC-rich layers

C/W multilayer structures were produced by sequential sputtering of C and W on Si single crystal substrate in Jozef Stefan Institut Ljubljana. Three different layer structures were produced which differed in the thicknesses and numbers of the individual layers. The initial thickness of the specimens was determined by cross sectional electron microscopy (XTEM): the structures were the followings: C 10.4 nm/W 24.5 nm/C 9.1 nm/Si substrate; C 8 nm/W 18 nm/C 8.7 nm/W 18.6 nm/C 7.1 nm/Si substrate; C 15.8 nm/W 22.7 nm/C 17.2 nm/W 24.3 nm/C 21.1 nm/Si substrate. For easier reference we will call them as 102010, 1020 and 2020 respectively.

The WC-rich layers were produced by irradiating the multilayer structures by Xe^+ or Ar^+ ions at room temperature in Helmholtz-Zentrum Dresden-Rossendorf. The fluences for xenon were 0.1–3 × 10^{16} Xe^+/cm^2 the applied energy was between 40 and 160 keV. For argon irradiation the fluences varied between 0.1 and 6 × 10^{16} Ar^+/cm^2 with energies in the range of 40–110 keV.

2.2. AES depth profiling

2.2.1. Evaluation of the AES depth profile

For determining the component in-depth distributions before and after the ion irradiation AES depth profiling has been performed. The detailed description of the AES depth profiling procedure can be found in Ref. [23]. Its summary is as follows. The Auger spectra were recorded by a STAIB DESA 150 pre-retarded Cylindrical Mirror Analyzer (CMA) in direct current mode. For depth profiling 1 keV Ar^+ ions were used with an angle of incidence of 65° with respect to the surface normal (for the "strange" angle of incidence see Ref. [23]). The ion current was kept constant during sputtering. The sample was rotated (6 rev/min) during ion bombardment. These parameters were chosen for minimizing the ion bombardment-induced surface and interface morphology changes [24].

The carbide formation was detected by the change of the C_{KLL} Auger peak shape, see Fig. 2 in Ref. [23]. The measured peak was decomposed to graphitic and carbide components by applying the Linear Least Square Solution (LLSS) built in CasaXPS program [25]. The relative sensitivity factor method [26] was used for the calculation of the atomic concentrations. The sputtering time was transformed to the removed thickness by applying our previously elaborated method [27]. The relative sputtering yields of pure C and Si could be determined from the sputtering times required to remove the known layer thicknesses of the as-deposited W and C layers. In the regions that contain mixed C and Si components (independently from their chemical state) we suppose that the total sputtering yield Y can be estimated as $Y = \Sigma X_i * Y_i$ where Y_i and X_i are the sputtering yield and concentration of component i (in our case 'C' or 'W'). All presented in-depth distributions were calculated by this procedure.

2.2.2. Artifact production

The AES depth profiling of the C/W system produces artifacts; thus the correction of the measured depth profiles is a paramount importance. In our recent paper [23] the artifact production had been discussed in details. Its essence is that due to the unavoidable intermixing, even at 1 keV Ar^+ bombardment (used in AES depth profiling for removal of the material) and the concomitant compound formation the depth profile of the pristine sample exhibits WC in the C/W interface region, which is evidently artifact since the XTEM studies verify that in the pristine sample there is an abrupt transition from the pure C to pure W (and vice versa) and there is no WC on the initial interface. It has been also shown that the sputter removal process can be described by TRIDYN simulation using default parameters. This simulation will be used to make correction by removing the artefacts of the experimentally measured depth profiles.

2.3. Corrosion test

2.3.1. Measurement

The corrosion resistance of the samples has been tested by potentiodynamic corrosion test in 3.5 wt% NaCl solution. The growth of the WC-rich layer started at the C/W interface and its thickness depended on the conditions of IBM. In the majority of the cases only a part of the top C layer was consumed by IBM-induced compound formation and thus, the sample surface contained a carbon layer of various thicknesses. Therefore, before the corrosion test we had to remove the carbon layer which covered the intermixed region. This was achieved by oxidation of the intermixed sample in microwave plasma for 10 min.

The electrochemical measurements were carried out at room temperature in a common electrochemical three-electrode glass cell. The potentiodynamic experiments were performed with a computer-controlled Gamry Reference 3000 potentiostat. A saturated calomel electrode (SCE) was the reference electrode which was immersed with the help of a Luggin capillary. A platinum mesh was applied as the counter electrode. The electrolyte solution was de-aerated 3.5 wt% NaCl solution prepared from analytical grade chemicals. The samples (with an effective area of 0.3 cm^2) were fixed with carbon glue to a stainless steel holder. The contact of the samples with the electrolyte was established by employing the hanging meniscus technique. The solution was purged with argon during 30 min before immersing the sample to reduce the dissolved-oxygen content in the solution. The polarization curves were recorded at constant sweep rate of 5 mV/min in a potential range of (−0.5)–(0.0) V vs. SCE. The polarization curves were characterized by the Tafel extrapolation method.

2.3.2. Evaluation of the corrosion tests

Pourbaix Diagrams can serve as useful guides for predicting stability under the expected pH and electrochemical potential (E) conditions.
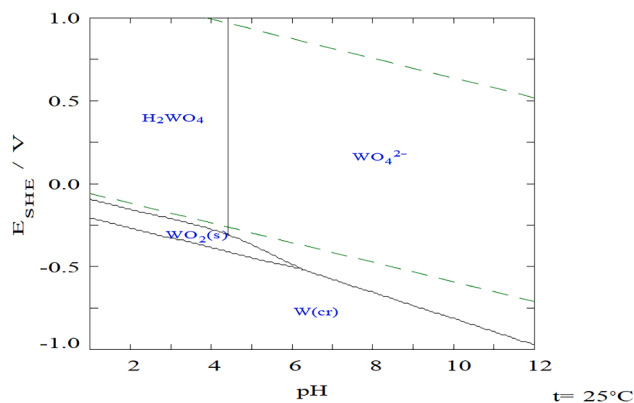
Fig. 1. Pourbaix diagram for tungsten prepared by Medusa software, $[WO_4^{2-}] = 10^{-6}$ M.

Fig. 1 shows the Pourbaix diagram for tungsten prepared by Medusa software [28,29]. The electrochemical potential is referred to the saturated hydrogen electrode (SHE). We can see that tungsten actively corrodes in the range of the applied potential (-0.744)–(-0.244) versus SHE at pH 7.

Moreover, the selective dissolution of carbides and tungsten phase in chlorine environment have been reported by several authors [7,30–32]. These findings suggest that the processes at the positive side of the voltammograms can be attributed to the dissolution of tungsten and tungsten carbide. The following electrochemical reactions are suggested [33–35]. The cathodic process in purged solution is H_2 evolution:

$$2H_2O + 2e^- \rightarrow H_2 + 2OH^- \tag{1}$$

The anodic process is the dissolution of tungsten and tungsten carbide:

$$W + 4H_2O \rightarrow WO_4^{2-} + 8H^+ + 6e^- \tag{2}$$

$$WC + 6H_2O \rightarrow WO_4^{2-} + CO_2 + 12H^+ + 10e^- \tag{3}$$
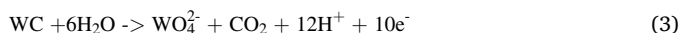
It should be also emphasized that the test is to be performed in bulk material. If during the test the corrosion consumes one of the layers and a new one appears, then the method still provides a useful number for the sample behavior but its meaning is restricted.

2.4. TRIDYN simulation and calculation of the formed amount of WC [22,23]

The TRIDYN simulation [21] is based on the binary collision approximation model for ballistic transport and the full cascade process simulation. In cases when the average atomic number is above 40, which is our present case, the mixing is governed by thermal spike model [36]. In this case the application of a simulation based on ballistic processes is questionable. Still we have shown that applying some parametrization it was possible to estimate the in-depth distribution of the elements after ion irradiation by using TRIDYN simulation. Setting the relocation threshold energy – determines the strength of the mixing – to 2 eV for all elements (C, W, Si) an excellent agreement between the experimental and simulated in-depth distributions were found [22].

The TRIDYN simulation cannot handle the compound formation. On the other hand, the experimental observations were similar to those in the case of the mixing of Si/C [37] which allows to make a simple model. The experimental observations: a./ unreacted W and C have only rarely found, b./ the WC concentration reached even 100% (in case of SiC it was only 80% [37]). Thus we assume that all minority C or W forms carbide and there is no limit in carbide formation.
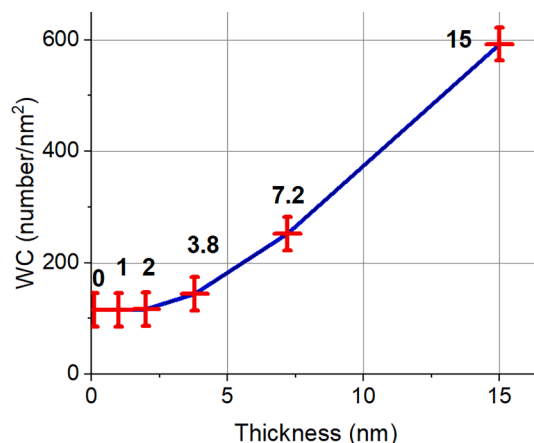

Fig. 2. The amount of WC provided by TRIDYN simulation of AES depth profiling (Ar^+, 1 keV, 65°) for structures of $C_{pure}/WC_{pure}/W_{pure}$. The x axis shows the thickness of the initial WC layer. The numbers in the figures show the initial thickness of the layers in nm-s.

3. Results and discussion

3.1. WC-rich layer production

The ion mixing and the concomitant WC formation starts at the interfaces and growth toward the originally pure layers resulting in various distributions. The shapes of the distributions strongly depend on the ion bombardment conditions and layer structure. In the following some examples of the observed distributions will be shown.

To start with it should be emphasized that the AES depth profiling produces artifacts, extended ion mixing and compound formation occurs at interfaces, as it is discussed in details in our recent paper [23]. The strength of artifact production strongly depends on the initial structure of the sample; the worst is in the case of pure layers. Anyhow the as received AES depth profiles should be carefully checked and should be corrected if it is necessary. As it was mentioned earlier the TRIDYN simulation, using default parameters, is applicable for the description of the depth profiling process. For the correction of the as received depth profiles we have developed a reverse process. We have assumed "initial" distributions and simulated the depth profile; by comparing the assumed "initial" distribution with the simulated one the artifact can be easily estimated. Fig. 2 shows the so called master curve. It was calculated assuming $C_{pure}/WC_{pure}/W_{pure}$ layer system, in which the transitions in the layers are abrupt and shows the simulated (experimentally measured) amount of WC as a function of the thickness of the initial WC layer.

Fig. 2 clearly shows that based on the amount of simulated (measured) WC we cannot distinguish between samples with initial structures of the pure C/W (0 nm thick WC) and C/2 nm WC/ W. It follows that our method, because of the artifact production is not applicable to reveal extreme thin WC layers. It should be added that the actual strength of the artefact production strongly depends on the type of transition and it is different for C/WC and WC/W transitions [23] and depends on the shape of distribution. The worst case is the abrupt transition; thus, Fig. 2 provides an overestimation of artefact production. Based on the above we conclude that if the amount of WC, produced by the high energy irradiation, is higher than 400 WC number/ nm^2 then the error introduced by the AES depth profiling is in the range of 10–15%. At lower values the error increases; we cannot even detect a 4 nm thick WC layer, since the WC produced on pure C/W transition is roughly the same. Thus, in the evaluation of the experimental we will follow a simple routine. All measured WC values will be given in Tables and in the text. Those which are lower than 350 (number/nm^2) will be given in parentheses emphasizing that the error of that value is

high might be even 100%. For WC values higher than 500 (number/ nm^2) we will suppose that the error is in the range of 10–15% but will not be given.

Fig. 3 shows typical carbide distributions. Note that besides the tungsten carbide, we are interested in, the substrate Si might also be intermixed with the last C layer, producing silicon carbide at the interface. In the following we will mainly deal with the WC production, which was produced by applying 120 keV xenon irradiation of various

fluences on sample of 102010. In the case of 1×10^{15} Xe$^+$/cm^2 (Fig. 3a) irradiation the carbide began to grow from the interfaces. With increasing fluence the two individual carbide regions just begin to overlap, see 2.5×10^{15} Xe$^+$/cm^2 (Fig. 3b) irradiation. After irradiation 5×10^{15} Xe$^+$/cm^2 (Fig. 3c) the place of this overlap can be only slightly recognized. Irradiation 10×10^{15} Xe$^+$/cm^2 (Fig. 3d) causes the formation of well-developed WC layer consuming practically all W. Since the WC formation terminated additional increase of fluence (30×10^{15} Xe$^+$/

(a) 1×10^{15} Xe$^+$/cm^2, 120 keV

(b) 2.5×10^{15} Xe$^+$/cm^2, 120 keV

(c) 5×10^{15} Xe$^+$/cm^2, 120 keV

(d) 10×10^{15} Xe$^+$/cm^2, 120 keV

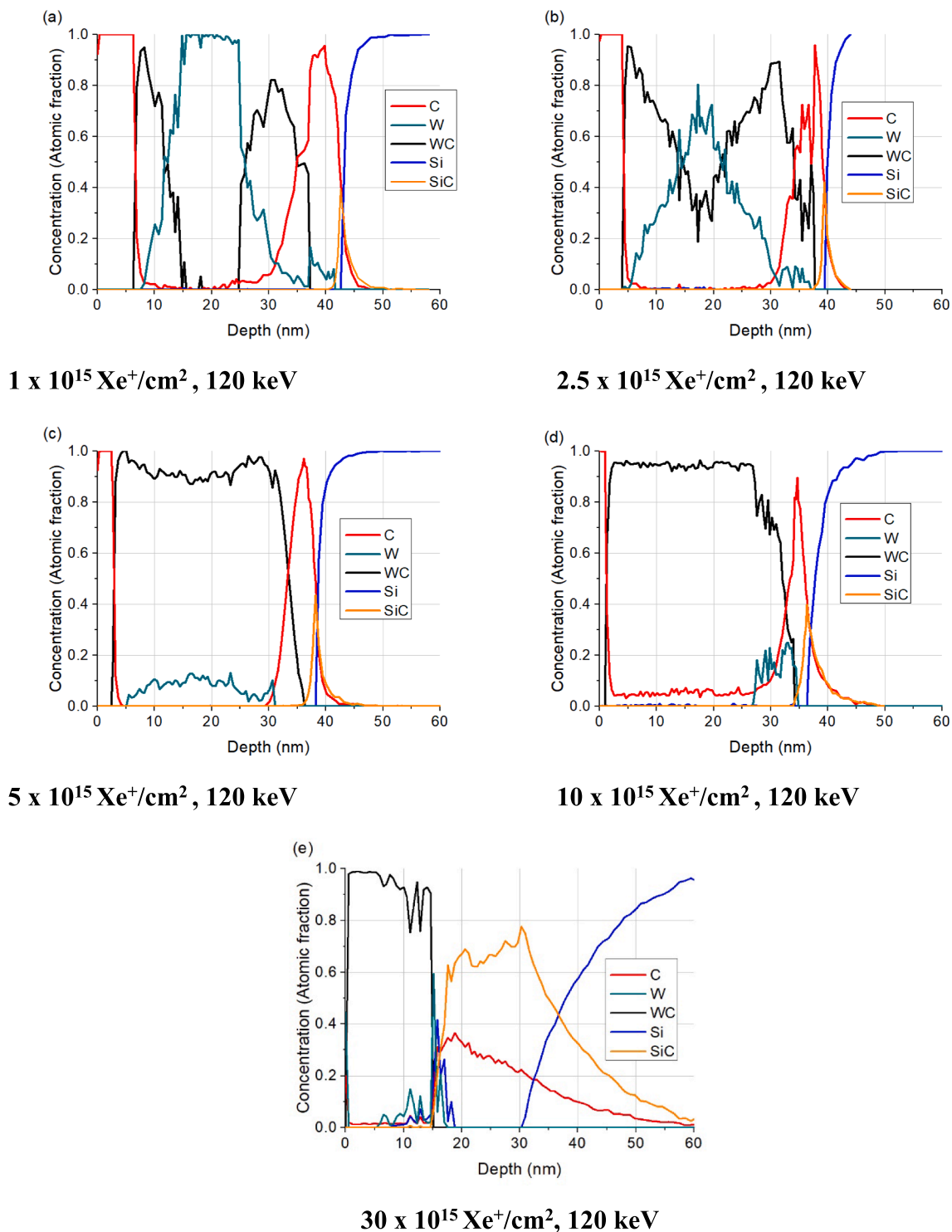(e) 30×10^{15} Xe$^+$/cm^2, 120 keV

Fig. 3. The in-depth distributions calculated from AES depth profiles of measured sample 102010 irradiated by 120 keV Xe$^+$ for fluences in units of 10^{15}Xe$^+$/cm^{2}a. 1; b. 2.5; c. 5; d. 10; e. 30.

cm^2) can only results in further intermixing of the Si substrate see Fig. 3e. In fact, the Si from the substrate is strongly intermixed with the reminder C and the WC layer as well. The intermixing results in high SiC formation which is made by consuming all the carbon but it also destroys the WC layer replacing W by Si. During this process besides the formation of SiC, which exhibits also a good chemical resistance [18,37], metallic W and Si appears in the WC and SiC layers, which corrupt the chemical resistance (see later) of the sample.

Similar distributions can be produced in several ways. E.g. by decreasing the irradiation energy to 40 keV and increasing the fluence to 2.5×10^{15} Xe$^+$/cm^2 a distribution similar to Fig. 3a can be produced as it is shown in Fig. 4. This happens despite of the big difference in the projected range of xenon ions at the two energies being 14 ± 3 nm and 25 ± 10 nm for the 40 and 120 keV energy, resp. calculated by SRIM [38].

Obviously the produced WC distribution can also be tuned by varying the initial layer structure. Fig. 5 shows an AES depth profile of a 1020 (C 8 nm/W 18 nm/C 8.7 nm/W 18.6 nm/C 7.1 nm/Si substrate) sample irradiated by 5×10^{15} Xe$^+$/cm^2, 160 keV. For this thicker structure higher irradiation energy, 160 keV Xe$^+$ (projected range 37 ± 19 nm [38]) was needed to produce a thick WC layer; the in-depth profile shows that the carbide layer produced is thicker than even the whole thickness of sample 102010.

A large variety of irradiation conditions have been applied on three layer structures providing a rich assembly of various WC carbide distribution. These samples have been tested for corrosion resistance.
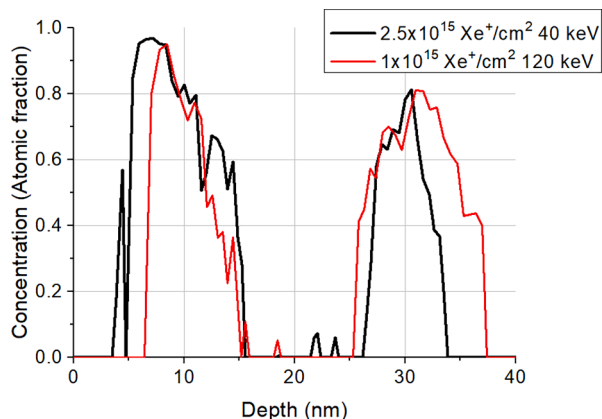

Fig. 4. WC in-depth distribution produced by irradiation sample 102010 after irradiation of 2.5×10^{15}Xe$^+$/cm^2 40 keV and 1×10^{15}Xe$^+$/cm^2 120 keV, resp.
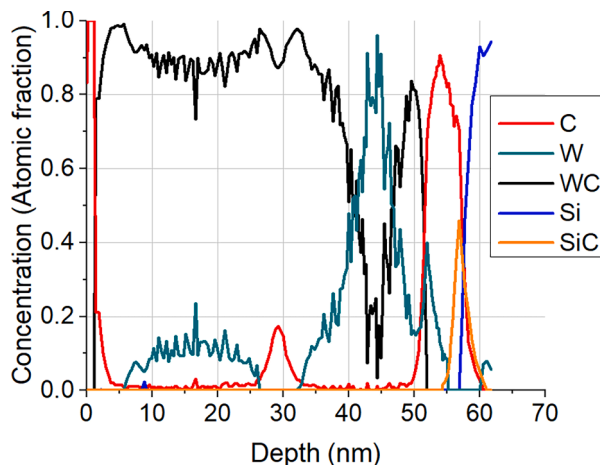

Fig. 5. AES in-depth distribution of irradiation 5×10^{15}Xe$^+$/cm^2, 160 keV, sample 1020.

3.2. Corrosion resistance

The corrosion resistance of the samples has been tested by potentiodynamic corrosion test in 3.5 wt% NaCl solution. We should also consider that this test might alter the sample. Thus, AES depth profiling has been performed on samples after the corrosion test for revealing what happened with the sample during the test. Fig. 6. a and b show the AES depth profiles recorded after performing the potentiodynamic test, on samples 102010 which had been irradiated by low (3×10^{15} Ar$^+$/cm^2) and high fluence (5×10^{15} Xe$^+$/cm^2) of 40 keV Ar$^+$ and 120 keV Xe$^+$, resp. For better comparison the depth profile of the similar non-tested sample is depicted in the figures, as well. The profiles were shifted to have the last carbon/Si substrate interface at the same depth.

It can be seen that in the case when the amount of produced WC is low (Ar$^+$ 40 keV 3×10^{15}/cm^2) the sample drastically altered during the test. These samples originally have low WC concentration and very high unreacted tungsten content. It can be seen that almost all tungsten component and the formed low amount of carbide present at the interfaces is completely dissoluted during the corrosion test. On the other hand, in the case of high fluence xenon irradiation the sample hardly changed during the test. This is due to the very low initial tungsten content and to the high concentration of corrosion resistive WC present in the sample.

The coating layers were built on Si substrate. The corrosion resistance of Si using this test is order of magnitude larger than that of the even perfect WC [39]. It is evident that if the layer degrades during the test and the Si surface is revealed the corrosion resistance suddenly strongly increases. Since such phenomenon has never been observed one can conclude that the substrate has not been involved in the process and thus the determined corrosion resistance is characteristic to the coating layer produced.

Fig. 7 shows some typical Tafel curves obtained for the different irradiated samples and different layer structures. The corrosion resistance of the sample can be ranged by the corrosion current density and corrosion potential derived from the Tafel extrapolation.

Fig. 7 shows that the results fall into two none overlapping ranges. From the Tafel curves the corrosion current densities have been calculated by applying the Tafel extrapolation. These values characterize the resistance against corrosion attack. The aim is to understand how the amount and/or distribution of the tungsten carbide produced by the various irradiations affect the corrosion resistance. Roughly speaking small and high amount of carbide results in low and high resistance against chemical attack. The medium region, cannot be easily understood, however; Fig. 8 describes the problem.

Fig. 8 shows three WC distributions produced by irradiation of a./ 120 keV Xe$^+$ 1×10^{15} /cm^2 b./120 keV Xe$^+$ 2.5×10^{15}/cm^2 on sample 102010 and 110 keV Ar$^+$ 3×10^{16}/cm^2 on sample 2020.

First of all, it is noted, that the WC distributions produced are in the range where the AES depth profiling artifact production is low, the error of the determination of the amount of WC is less than 15%, thus, the recorded depth profile does not need any correction. Similarly, potentiodynamic corrosion test does not affect the sample thus, the data can be safely discussed.

The three WC distributions show there steps of the WC layer formation process. In Fig. 8 a. the two WC layers, growing from neighbor interfaces, are just separated, while in Fig. 8 b they begin to overlap. Fig. 8c. shows the condition just before the termination of layer formation. The all over amount of WC in the first two cases is rather similar and in the third case is roughly 40% larger than the previous ones. The corrosion current densities in the first two cases are about 0.40 μA/cm^2, while in the third case it is 0.06 μA/cm^2. That is, the first two cases the resistance against corrosion is poor, while in the third case is excellent. This behavior had already been observed in the case SiC based protective layer produced by IBM [18], which led us to introduce the term effective areal density. The effective areal density, which determines the corrosion resistance, is to be calculated by integrating the amount of WC
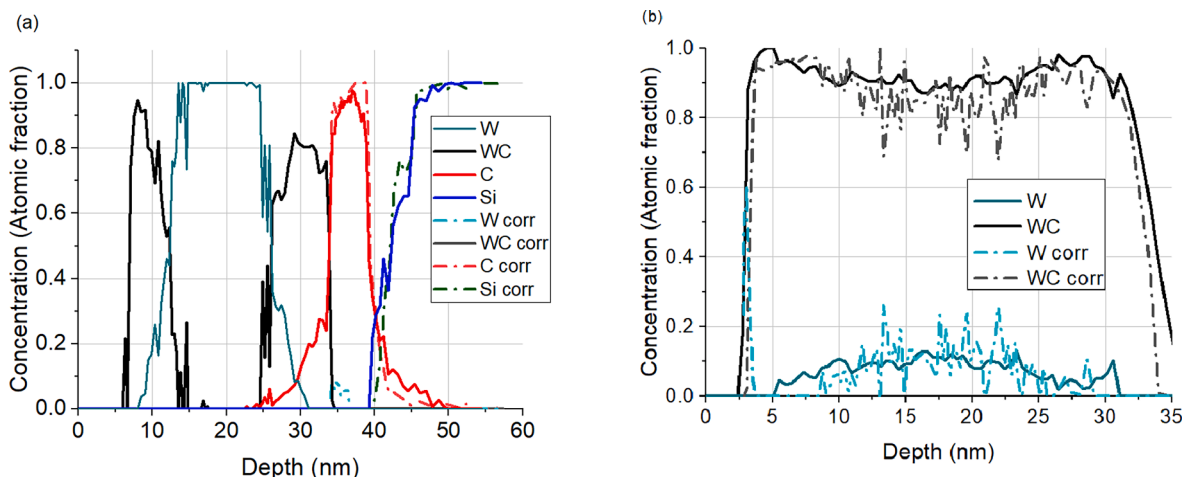
Fig. 6. AES depth profiles measured before and after the potentiodynamic test of sample 102010 irradiated by a. Ar$^+$ 40 keV 3 × 10^{15} /cm^2 and b. Xe$^+$ 120 keV 5 × 10^{15}/cm^2 b./.Note before the potentiodynamic test the sample is subjected a plasma treatment, thus the reminder of the upper C layer is removed.
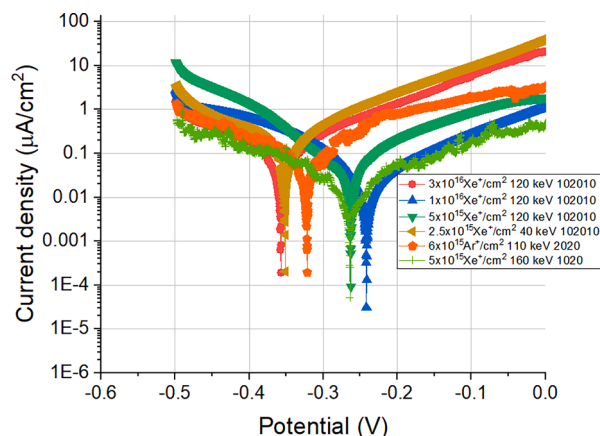

Fig. 7. Polarization curves obtained for some of the irradiated samples.

from that depth where its concentration exceeds a given value up to that depth where its concentration decreases below that certain values. This way before the overlap of the neighboring growing WC layers only the very first will be considered as the corrosion resistive layer. During the overlap procedure if the minimum value of the valley is under the pre-determined layer then the integration stops at that value (blue line in Fig. 8b), if the minimum is larger than the predetermined value then

integration goes further until the WC concentration decreases below the predetermined value. This predetermined value in the case of SiC is 20%, while in the case of WC it is 50%. It should be emphasized that this definition results in sharp increase of the effective areal density during the overlapping process. Really slight increase of the irradiation fluence results in the increase of the minimum between the two growing WC layers above the predetermined value, when the amount of the WC in the second layer is to be added to the first one resulting a great increases of the effective areal density. Now it will be checked how does this behavior is reflected in the corrosion resistance of the layer.

Table 1 shows the shapes of WC distributions, effective areal densities calculated as above, and the corrosion current densities for all measurements.

The experimental results have been listed according to the increasing values of the effective areal densities. We have chosen this representation since our aim is to find correlation between the corrosion resistance, which is inversely proportional with the corrosion current densities, and the effective areal density. In the Table we do not provide the shape of the 102010 3 × 10^{16} Xe$^+$/cm^2 120 keV irradiation (signed with *) as this irradiation caused the deterioration of the formed tungsten carbide (see Fig. 3e) resulting in worsening corrosion resistance. The graphical representation of all measured data (except the signed experiment) in Table 1 is shown in Fig. 9.

Both Table 1 and Fig. 9 show that the corrosion current densities are grouping into distinct regions; in Fig. 9 the blue vertical line divides the two regions, while in Table 1 the horizontal line is the border.
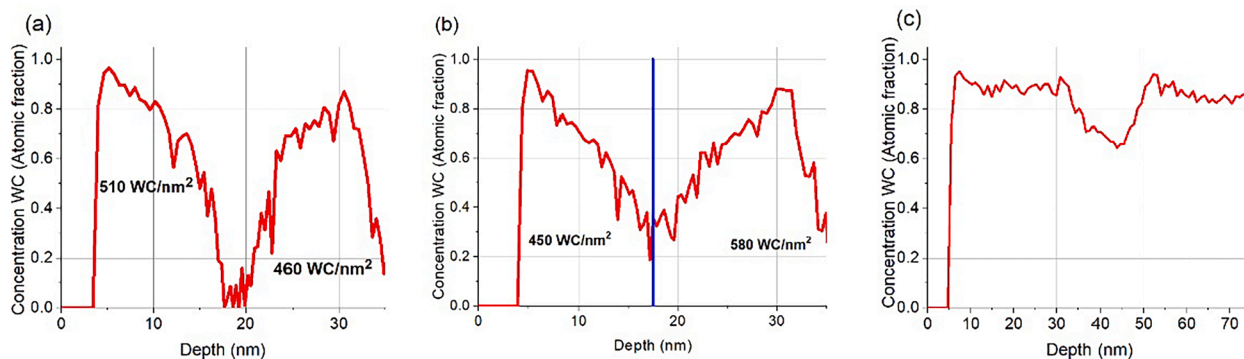

Fig. 8. The experimentally measured WC distributions after irradiation of a./102010 sample by 120 keV Xe$^+$ 1 × 10^{15}/cm^2 and b./120 keV Xe$^+$ 2.5 × 10^{15}/cm^2 and c./sample 2020 by 110 keV Ar$^+$ 3 × 10^{16}/cm^2. The areal densities of WC determined in the shown regions are given in the Fig. in WC number/nm^2 units. The blue line in Fig. 8b. shows the limit of integration. The corrosion current densities for samples in Fig. 8. a, b, c are 0.44, 0.40, 0.06 µA/cm^2. (For interpretation of the references to colour in this figure legend, the reader is referred to the web version of this article.)

Table 1

The shapes of WC distributions, WC effective areal density and corrosion current densities, determined of various samples after the various IBM (first column). The shape of the WC distribution in experiment designed by* is different from that shown in column 2, thus it is discussed separately.

Sample & irradiation	Shape of WC distribution	WC effective areal density (numb/nm²)	Corrosion current density, j_{corr} (μA/cm²)
102010 1×10^{15} Ar⁺/cm² 40 keV		(169)	0.44
1020 3×10^{15} Ar⁺/cm² 80 keV		(247)	0.49
102010 3×10^{15} Ar⁺/cm² 40 keV		(248)	0.45
102010 1×10^{15} Xe⁺/cm² 120 keV		(282)	0.44
1020 3×10^{15} Ar⁺/cm² 50 keV		(289)	0.5
102010 2.5×10^{15} Xe⁺/cm² 40 keV		425	0.49
2020 6×10^{15} Ar⁺/cm² 110 keV		469	0.26
102010 1×10^{16} Ar⁺/cm² 40 keV		512	0.42
102010 2.5×10^{15} Xe⁺/cm² 120 keV		450	0.40
102010 3×10^{16} Xe⁺/cm² 120 keV*		1223	0.19
102010 5×10^{15} Xe⁺/cm² 120 keV		1407	0.09
102010 1×10^{16} Xe⁺/cm² 120 keV		1457	0.06
102010 3×10^{16} Ar⁺/cm² 40 keV		1567	0.13
1020 5×10^{15} Xe⁺/cm² 160 keV		2370	0.06
1020 3×10^{16} Ar⁺/cm² 80 keV		2570	0.13
2020 3×10^{16} Ar⁺/cm² keV		3408	0.05
2020 6×10^{16} Ar⁺/cm² 110 keV		3553	0.06

First we deal with the region with effective carbide density lower than 550 WC (number/nm²). Let us recall that below 350 WC, the AES depth profiling provides data with terrible high scatter, see Fig. 1; the determination of the initial WC distribution is practically impossible. The only thing which we know is that larger amount of measured WC means larger amount of initial WC. Moreover, considering that the corrosion test alters the sample in case of thin WC layer (produced by the IBM) the measured corrosion current density is not characteristic to the WC layer but to the sample. Accordingly, the data below 350 WC (number/nm²) belonging to the first range in Table 1 and/or Fig. 9. should be considered with great care. Consequently, any reasonable dependence between the effective areal density and corrosion current density cannot be established. Rather this region can be characterized as: the corrosion current density is 0.5 (μA/cm²) ± 35% if the effective areal density is in the range of 0–550 WC (number/nm²).

Considering the other, the lower range, of the corrosion current density, first we must emphasize that in this range either the AES depth profiling or the corrosion test are accurate enough. Thus, here if large scatter appears as it will, its cause is not the noisy measurement but the very feature of the samples. Concerning the correlation between the corrosion current density and the effective areal density the conclusion is similar as before; we cannot establish any correlation between the amount of WC and corrosion current density. To characterize the region,
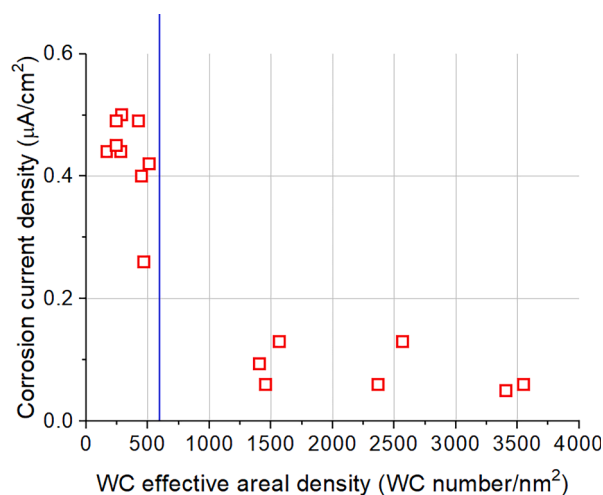
nm²) the corrosion current density is 0.08 (μA/cm²) ± 36%. The large scatter means that the amount/shape of WC alone does not fully determine the corrosion resistance. Most likely the various defects like pin holes, solute W etc. also contribute to the corrosion resistance but their effect is considerable less than that of the WC.

For a better understanding of the formation of the two distinct regions of the corrosion resistance values we consider the fluence dependence of the corrosion resistance. To do this in Fig. 10 the areal density, the effective areal density and the corrosion current density is shown for sample 102010 in the case of 120 keV Xe⁺ irradiation.

The areal density is the integral of an element, compound along the depth from the surface. In our present case at the beginning it is the sum of the WC units being in the two separate layers growing from the C/W and W/C interfaces. It is growing continuously with the fluence until it reaches a saturation value. On the other hand, the corrosion current density is a kind of step function. Thus, it is clear that between the two quantities (areal density, corrosion resistance) cannot be established any connection. This is why we introduced the term effective areal density. This quantity also shows a sudden jump when during the coalescence of the two neighboring layers a user defined value of the minimal concentration between the separating valley is reached. Seemingly, the structural change nicely correlates with the increase of the corrosion resistance. What could be the reason for this behavior?

It should be recalled that in disordered solids the etching shows percolation behavior [40] as a function of randomness. In this mainly
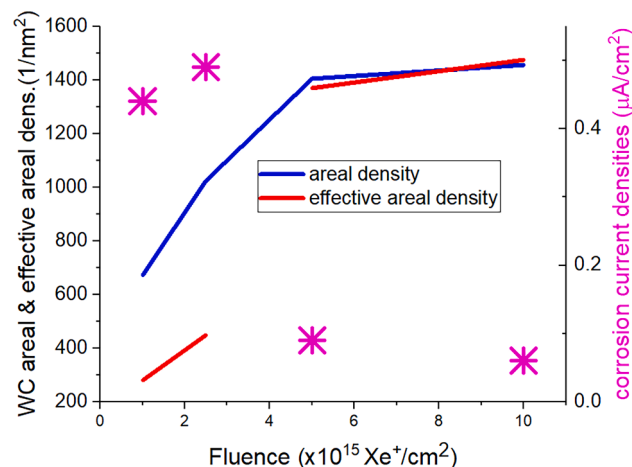

Fig. 9. Corrosion current density vs effective areal density.

we can say if the effective areal density is larger than 1200 WC (number/

Fig. 10. Areal density, effective areal density and corrosion current density vs the irradiation fluence curves. Sample 102010; irradiation Xe⁺ 120 keV.

Table 2
The corrosion current densities measured by various bulk materials applying potentiodynamic corrosion test in 3.5 wt% NaCl [41].

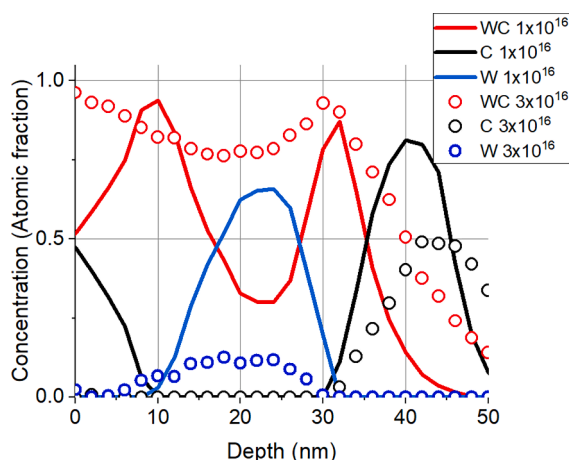| Material	Corrosion current density ($\mu A/cm^2$)
Mild steel	12.0 [41]
Tool steel	6.5 [41]
Grey cast iron	3.57 [41]
Copper	2.0 [41]
Brass	1.0 [41]
SS 163L	0.38 [41]
SS 304	0.38 [41]
SS Zeron	0.21 [41]
WC-10Co	1.84^{present}
WC made by IBM on Si	0.09^{present}

Fig. 11. The simulated in-depth profiles after irradiation of sample 102010 by Ar^+ ions. Irradiation conditions: 40 keV 1×10^{16} Ar^+ and 3×10^{16} Ar^+/cm^2.

amorphous structure the randomness can be represented by structural defects, solute metal (W) atoms, density fluctuation, etc. which might affect the etching rate. The shapes of the coalescences for the various irradiations, sample structures are rather similar thus a single value of the minimal concentration of the separating valley is sufficient to characterize it. During the coalescence the predetermined concentration value gives the percolation threshold which causes a sharp transition of the etching rate.

The behavior of the present system is similar to that of the SiC [18]. The only difference is the value of the minimum concentration determining the jump position of the effective areal density; it is 20% and 50% for SiC and WC, respectively.

To provide a ballpark estimate of these data, in Table 2 some corrosion current densities are shown measured by the same test on various materials.

Table 2 shows that our coating produced by IBM exhibit excellent resistance against chemical attack, eg. it is even better than specially prepared stainless steel. In Table 2 we also show measured data for a commercially available cermet coating (WC-10Co), its corrosion resistance is orders of magnitudes worse than the WC produced by IBM. This is mainly due to the preferential corrosion of the Co binder.

3.3. Design of protective coating

The experiments clearly show that in the C/W system the IBM produces tungsten carbide. That amount of tungsten carbide, which determines the corrosion resistance is measured by the effective area density of the WC; thus to design a coating layer with given corrosion resistance the effective areal density of WC should be designed. This can be done since in our recent paper [22] we have shown that the TRIDYN

code despite of the thermal spike mixing of the W/C system with proper parametrization provides a fair estimate of the IBM and the compound formation can also be calculated. This calculation also showed how can one choose proper parameters to build the same effective areal density starting from vastly different initial conditions. This gives a considerable freedom for the user. E.g. Fig. 3.c shows that applying irradiation of $5 \times 10^{15} Xe^+/cm^2$, 120 keV on sample 102010 produces a well-defined WC carbide layer having a corrosion current density of 0.09 $\mu A/cm^2$. What can we do if only Ar^+ is available? We can perform the TRIDYN simulation checking the WC formation for various fluences; Fig. 11 shows the result for $1 \times 10^{16} Ar^+$ and $3 \times 10^{16} Ar^+/cm^2$ of 40 keV irradiation, respectively. It shows that using 40 keV Ar^+ $1 \times 10^{16}/cm^2$ fluence is insufficient but increasing to $3 \times 10^{16}/cm^2$ a well-developed WC layer forms very similar to that shown in Fig. 3c.

We should, however, remember that while in the case of Si/C system the TRIDYN simulation describes the IBM by reasonable accuracy in the case of C/W system it gives only a fair estimate. Moreover, the inaccuracy of the method is the worst in that condition when the individual WC layers begin to overlap. Still perhaps slightly overestimated irradiation conditions can be found which provide the desired WC distribution.

4. Conclusions

C/W multilayer structures were irradiated by xenon and argon ions of energy and fluences of 40–120 keV and 0.1–6 $\times 10^{16}$ ions/cm², resp. The concentration in-depth distributions were measured by AES depth profiling, which proved that WC was produced by the irradiation. The amount of WC depended on the irradiation conditions (projectile, energy, fluence) and layer structure. The corrosion resistance of the irradiated samples has been tested by potentiodynamic corrosion test. The corrosion resistance could be characterized by the effective areal density of the WC. Having these layer structures and irradiation parameters the corrosion current density showed an interesting feature; if the effective areal density was in the range of 0–550 WC (number /nm²) the corrosion current density was 0.5 ($\mu A/cm^2$) $\pm$ 35%, while if the effective areal density was higher than 1200 WC (number/nm²) the corrosion current density was 0.08 ($\mu A/cm^2$) $\pm$ 36%, which was better than that of stainless steel. The effective areal density values can be calculated applying TRIDYN simulation. Thus, this fast and cheap simulation enables the design of custom made WC-rich coating layers.

CRediT authorship contribution statement

A.S. Racz: Conceptualization, Methodology, Investigation, Formal analysis, Validation, Visualization, Project administration, Funding acquisition, Writing - original draft, Writing - review & editing. **Z. Kerner:** Resources, Project administration, Writing - original draft. **M. Menyhard:** Conceptualization, Methodology, Formal analysis, Validation, Visualization, Writing - original draft, Writing - review & editing.

Declaration of Competing Interest

The authors declare that they have no known competing financial interests or personal relationships that could have appeared to influence the work reported in this paper.

References

[1] N. Nemati, M. Bozorg, O.V. Penkov, D.-G. Shin, A. Sadighzadeh, D.-E. Kim, Functional multi-nanolayer coatings of amorphous carbon/tungsten carbide with exceptional mechanical durability and corrosion resistance, ACS Appl. Mater. Interfaces. 9 (2017) 30149–30160, https://doi.org/10.1021/acsami.7b08565.

[2] J. Esteve, G. Zambrano, C. Rincon, E. Martinez, H. Galindo, P. Prieto, Mechanical and tribological properties of tungsten carbide sputtered coatings, Thin Solid Films. 373 (2000) 282–286, https://doi.org/10.1016/S0040-6090(00)01108-1.

[3] E.C. Weigert, M.P. Humbert, Z.J. Mellinger, Q. Ren, T.P. Beebe, L. Bao, J.G. Chen, Physical vapor deposition synthesis of tungsten monocarbide (WC) thin films on different carbon substrates, J. Vac. Sci. Technol. Vac. Surf. Films. 26 (1) (2008) 23–28.

[4] J. Pu, D. He, L. Wang, Effects of WC phase contents on the microstructure, mechanical properties and tribological behaviors of WC/a-C superlattice coatings, Appl. Surf. Sci. 357 (2015) 2039–2047, https://doi.org/10.1016/j.apsusc.2015.09.181.

[5] C. Rincón, G. Zambrano, A. Carvajal, P. Prieto, H. Galindo, E. Martínez, A. Lousa, J. Esteve, Tungsten carbide/diamond-like carbon multilayer coatings on steel for tribological applications, Surf. Coat. Technol. 148 (2-3) (2001) 277–283.

[6] T. Miller, L. Pirolli, F. Deng, C. Ni, A.V. Teplyakov, Structurally different interfaces between electrospark-deposited titanium carbonitride and tungsten carbide films on steel, Surface and Coatings Technology 258 (2014) 814–821.

[7] P.K. Katiyar, N.S. Randhawa, A comprehensive review on recycling methods for cemented tungsten carbide scraps highlighting the electrochemical techniques, Int. J. Refract. Met. Hard Mater. 90 (2020) 105251, https://doi.org/10.1016/j.ijrmhm.2020.105251.

[8] B. Han, S. Zhu, W. Dong, Y. Bai, H. Ding, Y. Luo, P. Di, Improved mechanical performance and electrochemical corrosion of WC-Al2O3 composite in NaCl solution by adding the TiC additives, Int. J. Refract. Met. Hard Mater. 99 (2021) 105566, https://doi.org/10.1016/j.ijrmhm.2021.105566.

[9] R. Ali, M. Sebastiani, E. Bemporad, Influence of Ti–TiN multilayer PVD-coatings design on residual stresses and adhesion, Mater. Des. 75 (2015) 47–56, https://doi.org/10.1016/j.matdes.2015.03.007.

[10] F. Zhu, Z. Chen, K. Liu, W. Liang, Z. Zhang, Deposition of thin tungsten carbide films by dual ion beam sputtering deposition, Vacuum. 157 (2018) 45–50, https://doi.org/10.1016/j.vacuum.2018.08.023.

[11] T. Zhang, C. Ji, J. Shen, J. Yang, J. Chen, Y. Gao, G. Sun, Surface modification of steel by high-dose pulse-ion implantation of titanium, tungsten, molybdenum and carbon, Nucl. Instrum. Methods Phys. Res. Sect. B Beam Interact. Mater. At. 59–60 (1991) 828–832, https://doi.org/10.1016/0168-583X(91)95713-N.

[12] C. Liu, M. Xu, W. Zhang, S. Pu, P.K. Chu, Effects of tungsten pre-implanted layer on corrosion and electrochemical characteristics of amorphous carbon films on stainless steel, Diam. Relat. Mater. 17 (2008) 1738–1742, https://doi.org/10.1016/j.diamond.2008.01.114.

[13] P. Sigmund, A. Gras-Marti, Theoretical aspects of atomic mixing by ion beams, Nucl. Instrum. Methods. 182–183 (1981) 25–41, https://doi.org/10.1016/0029-554X(81)90668-6.

[14] R. Escobar Galindo, N. Benito, D. Duday, G.G. Fuentes, N. Valle, P. Herrero, L. Vergara, V. Joco, O. Sanchez, A. Arranz, C. Palacio, In-depth multi-technique characterization of chromium–silicon mixed oxides produced by reactive ion beam mixing of the Cr/Si interface, J. Anal. At. Spectrom. 27 (2012) 390, https://doi.org/10.1039/c2ja10296j.

[15] S. Gupta, D.C. Agarwal, S.A. Khan, S. Neeleshwar, S. Ojha, S. Srivastava, A. Tripathi, S. Amirthapandian, B.K. Panigrahi, D.K. Avasthi, PbTe nanocrystal formation by interface mixing of Te/Pb bilayer using low energy ions, Mater. Sci. Eng. B. 184 (2014) 58–66, https://doi.org/10.1016/j.mseb.2014.01.002.

[16] A. Arranz, C. Palacio, Nanoscale reactive ion beam mixing of Ti/Si and Si/Ti interfaces, Thin Solid Films. 515 (2007) 3426–3433, https://doi.org/10.1016/j.tsf.2006.10.005.

[17] F. Harbsmeier, W. Bolse, A.-M. Flank, Ion beam induced solid state reaction in Si/C layer systems, Nucl. Instrum. Methods Phys. Res. Sect. B Beam Interact. Mater. At. 178 (2001) 214–219, https://doi.org/10.1016/S0168-583X(00)00461-4.

[18] A.S. Racz, Z. Kerner, A. Nemeth, P. Panjan, L. Peter, A. Sulyok, G. Vertesy, Z. Zolnai, M. Menyhard, Corrosion resistance of nanosized silicon carbide-rich composite coatings produced by noble gas ion mixing, ACS Appl. Mater. Interfaces. 9 (2017) 44892–44899, https://doi.org/10.1021/acsami.7b14236.

[19] A.S. Racz, D. Zambo, G. Dobrik, I. Lukacs, Z. Zolnai, A. Nemeth, P. Panjan, A. Deak, G. Battistig, M. Menyhard, Novel method for the production of SiC micro and nanopatterns, Surf. Coat. Technol. 372 (2019) 427–433, https://doi.org/10.1016/j.surfcoat.2019.05.061.

[20] A.S. Racz, D. Dworschak, M. Valtiner, M. Menyhard, Scratching resistance of SiC-rich nano-coatings produced by noble gas ion mixing, Surf. Coat. Technol. 386 (2020) 125475, https://doi.org/10.1016/j.surfcoat.2020.125475.

[21] W. Möller, W. Eckstein, Tridyn — a TRIM simulation code including dynamic composition changes, Nucl. Instrum. Methods Phys. Res. Sect. B Beam Interact. Mater. At. 2 (1984) 814–818, https://doi.org/10.1016/0168-583X(84)90321-5.

[22] A.S. Racz, Z. Fogarassy, U. Kentsch, P. Panjan, M. Menyhard, Design and production of tungsten-carbide rich coating layers, Appl. Surf. Sci. 586 (2022) 152818, https://doi.org/10.1016/j.apsusc.2022.152818.

[23] A.S. Racz, Z. Fogarassy, P. Panjan, M. Menyhard, Evaluation of AES depth profiles with serious artefacts in C/W multilayers, Appl. Surf. Sci. 582 (2022) 152385, https://doi.org/10.1016/j.apsusc.2021.152385.

[24] M. Menyhard, High-depth-resolution Auger depth profiling/atomic mixing, Micron 30 (1999) 255–265, https://doi.org/10.1016/S0968-4328(99)00010-4.

[25] N. Fairley, A. Carrick, N. Fairley, Recipes for XPS Data Processing, Acolyte Science, Knutsford, 2005.

[26] K.D. Childs, C.L. Hedberg, Physical Electronics, Incorporation, eds., Handbook of Auger electron spectroscopy: a book of reference data for identification and interpretation in Auger electron spectroscopy, 3rd ed., Physical Electronics, Eden Prairie, 1995.

[27] L. Kotis, M. Menyhard, A. Sulyok, G. Sáfrán, A. Zalar, J. Kovač, P. Panjan, Determination of the relative sputtering yield of carbon to tantalum by means of Auger electron spectroscopy depth profiling, Surf. Interface Anal. 41 (2009) 799–803, https://doi.org/10.1002/sia.3101.

[28] R.S. Lillard, G.S. Kanner, D.P. Butt, The nature of oxide films on tungsten in acidic and alkaline solutions, J. Electrochem. Soc. 145 (8) (1998) 2718–2725.

[29] I. Puigdomenech, Medusa software, Chemical equilibrium diagrams, KTH. (n.d.). <https://www.kth.se/che/medusa/downloads-1.386254> (Accessed April 5, 2022).

[30] I.-W. Sun, A.G. Edwards, G. Mamantov, Spectroscopic and electrochemical studies of tungsten(VI) and tungsten(V) chloride and oxychloride complexes in a sodium chloride saturated sodium chloroaluminate melt, J. Electrochem. Soc. 140 (10) (1993) 2733–2739.

[31] Q. Zhang, X. Xi, Z. Nie, L. Zhang, L. Ma, Electrochemical dissolution of cemented carbide scrap and electrochemical preparation of tungsten and cobalt metals, Int. J. Refract. Met. Hard Mater. 79 (2019) 145–153, https://doi.org/10.1016/j.ijrmhm.2018.12.001.

[32] S. Hochstrasser(-Kurz), Y. Mueller, C. Latkoczy, S. Virtanen, P. Schmutz, Analytical characterization of the corrosion mechanisms of WC–Co by electrochemical methods and inductively coupled plasma mass spectroscopy, Corros. Sci. 49 (4) (2007) 2002–2020.

[33] B. Han, W. Dong, B. Fan, S. Zhu, Comparison on the immersion corrosion and electrochemical corrosion resistance of WC–Al$_2$O$_3$ composites and WC–Co cemented carbide in NaCl solution, RSC Adv. 11 (2021) 22495–22507, https://doi.org/10.1039/D1RA03549E.

[34] E. Patrick, M.E. Orazem, J.C. Sanchez, T. Nishida, Corrosion of tungsten microelectrodes used in neural recording applications, J. Neurosci. Methods. 198 (2011) 158–171, https://doi.org/10.1016/j.jneumeth.2011.03.012.

[35] V.A.D. Souza, A. Neville, Mechanisms and kinetics of WC-Co-Cr high velocity oxy-fuel thermal spray coating degradation in corrosive environments, J. Therm. Spray Technol. 15 (2006) 106–117, https://doi.org/10.1361/105996306X92677.

[36] M. Seita, R. Schäublin, M. Döbeli, R. Spolenak, Selective ion-induced grain growth: thermal spike modeling and its experimental validation, Acta Mater. 61 (2013) 6171–6177, https://doi.org/10.1016/j.actamat.2013.06.056.

[37] A.S. Racz, M. Menyhard, Design of corrosion resistive SiC nanolayers, ACS Appl. Mater. Interfaces. 10 (2018) 22851–22856, https://doi.org/10.1021/acsami.8b06425.

[38] SRIM Stopping and range of ions in matter by Ziegler, J. F. version SRIM, 2013 Software freely available www.srim.org., n.d.

[39] E. Ilic, A. Pardo, R. Hauert, P. Schmutz, S. Mischler, Silicon corrosion in neutral media: the influence of confined geometries and crevice corrosion in simulated physiological solutions, J. Electrochem. Soc. 166 (2019) C125–C133, https://doi.org/10.1149/2.0241906jes.

[40] K.M. Kolwankar, M. Plapp, B. Sapoval, Percolation-dependent reaction time in the etching of disordered solids, Europhys. Lett. EPL. 62 (2003) 519–525, https://doi.org/10.1209/epl/i2003-00382-3.

[41] C.T. Kwok, F.T. Cheng, H.C. Man, Synergistic effect of cavitation erosion and corrosion of various engineering alloys in 3.5% NaCl solution, Mater. Sci. Eng. A. 290 (2000) 145–154, https://doi.org/10.1016/S0921-5093(00)00899-6.